TU Delft

Delft University of Technology

A combined microstructural, electrochemical and nanomechanical study of the corrosion and passivation properties of a Cr/CrN multilayer coating

Rahimi, Ehsan; Nijdam, Thijs; Jahagirdar, Adwait; Broitman, Esteban; Mol, Arjan

DOI
10.1016/j.corsci.2025.112943

Publication date
2025

Document Version
Final published version

Published in
Corrosion Science

Citation (APA)
Rahimi, E., Nijdam, T., Jahagirdar, A., Broitman, E., & Mol, A. (2025). A combined microstructural, electrochemical and nanomechanical study of the corrosion and passivation properties of a Cr/CrN multilayer coating. *Corrosion Science*, *252*, Article 112943. https://doi.org/10.1016/j.corsci.2025.112943

Important note
To cite this publication, please use the final published version (if applicable).
Please check the document version above.

Copyright
Other than for strictly personal use, it is not permitted to download, forward or distribute the text or part of it, without the consent of the author(s) and/or copyright holder(s), unless the work is under an open content license such as Creative Commons.

Takedown policy
Please contact us and provide details if you believe this document breaches copyrights.
We will remove access to the work immediately and investigate your claim.

This work is downloaded from Delft University of Technology.
For technical reasons the number of authors shown on this cover page is limited to a maximum of 10.

Corrosion Science 252 (2025) 112943

Contents lists available at ScienceDirect

Corrosion Science

journal homepage: www.elsevier.com/locate/corsci

A combined microstructural, electrochemical and nanomechanical study of the corrosion and passivation properties of a Cr/CrN multilayer coating

Ehsan Rahimi [a,*,1,2,3], Thijs Nijdam [b], Adwait Jahagirdar [b], Esteban Broitman [b], Arjan Mol [a]

[a] Delft University of Technology, Department of Materials Science and Engineering, Mekelweg 2, Delft 2628 CD, the Netherlands
[b] SKF Research & Technology Development, Houten 3992 AE, the Netherlands

ARTICLE INFO

Keywords:
PVD, CrN, Cr/CrN Multilayer
Nanomechanical
Nanoindentation
Passivation
Electrochemical analyses
Corrosion

ABSTRACT

This research provides detailed insights into the correlation of microstructural and morphological characteristics of a Cr/CrN multilayer coating deposited onto steel and its corrosion behavior, by examining its local surface electronic properties, nanomechanical behavior, and electrochemical activity in a 3.5 % NaCl solution. A key focus of the study is the influence of physicochemical surface evolution on nano-mechanical properties of Cr/CrN coating. This is investigated by correlating electrochemical data from electrochemical impedance spectroscopy (EIS) with findings from X-ray photoelectron spectroscopy (XPS) and nanoindentation analysis. The integrated approach shed light on physicochemical evolution of the coating, and its resistance to corrosion in demanding environments.

1. Introduction

Transition metal nitride coatings are widely recognized as promising materials for enhancing the performance and extending the service life of tools, particularly under extreme conditions such as marine environments [1], elevated temperatures [2], simulated body fluids [3], and high-pressure aqueous environments [4]. These performance advantages are linked to their high hardness, elevated elastic modulus, low friction coefficient, excellent durability against wear and corrosion, and excellent adhesion to steel surfaces [5–7]. These hard coatings are commonly deposited using advanced techniques, including physical vapor deposition (PVD) methods such as magnetron sputtering [8], and chemical vapor deposition (CVD) [9]. Among the various transition metal nitride coatings, chromium nitride (CrN) has drawn global interest thanks to its excellent mechanical properties and robust resistance to corrosion and oxidation [10] as well as high-temperature oxidation [11].

The CrN-based coatings exhibit remarkable corrosion resistance due to the spontaneous formation of a passive chromium oxide layer, even when exposed to highly corrosive environments. However, in environments containing aggressive ions (Cl^- and SO_4^{2-}, etc.) or under tribocorrosion conditions, this protective oxide layer can be easily degraded, resulting in accelerated corrosion [6,10]. Despite the high chemical stability of the CrN ceramic phase (*Fm-3m*) the PVD CrN coatings remain prone to defects such as pinholes, which can serve as initiation sites for localized corrosion, potentially accelerating further degradation [12]. To achieve superior performance in metal nitride coatings, a variety of advanced microstructural designs have been developed, including multi-element composites, gradient transitional microstructures, multilayered coating architectures, and the combination of nanocrystalline and amorphous phases [13–15]. To address the tribological and corrosion challenges associated with CrN-coated substrates, attempts were made to incorporate additional elements and design multilayer structures such as CrN/CrAlN [16], CrN/ZrN [17], CrN/NbN [18], TiAlN/CrN [19], CrN/Mo_2N [20] and CrN/W_2N [20], CrN/TiN [21], CrN/TiSiN [22].

A Cr/CrN multilayer structure has been shown to significantly enhance the corrosion resistance of CrN coatings [14,23]. Consequently, this multilayer system is expected to exhibit excellent mechanical properties, a dense and uniform surface, and superior corrosion resistance. The performance of a Cr/CrN multilayer coating is strongly dependent on its architecture. For instance, the work by Chipatecua

* Corresponding author.
E-mail address: e.rahimi-2@tudelft.nl (E. Rahimi).
[1] ORCID ID: 0000–0002-7128–8940
[2] Google scholar: https://scholar.google.com/citations?user=pNVxwcYAAAAJ&hl=en
[3] Web of Science ResearcherID: I-8386–2019

https://doi.org/10.1016/j.corsci.2025.112943
Received 14 February 2025; Received in revised form 20 March 2025; Accepted 13 April 2025
Available online 15 April 2025
0010-938X/© 2025 The Author(s). Published by Elsevier Ltd. This is an open access article under the CC BY license (http://creativecommons.org/licenses/by/4.0/).

et al. [24] emphasized the importance of the total thickness and bilayer period for optimizing corrosion resistance. Their findings showed that Cr/CrN coatings with a lower thickness and a shorter bilayer period exhibited superior corrosion resistance. In another study, Wang et al. explored the corrosion and tribocorrosion performance of two-layer and multi-layer Cr/Cr_xN coatings [25]. They observed that the multi-layer Cr/Cr_xN coating exhibited a greater number of transverse interfaces, which were marked by a flat and densely packed structure. Additionally, their electrochemical impedance spectroscopy (EIS) measurements indicated that the multilayer coating had a charge transfer resistance thirteen orders of magnitude higher than the two-layer coating. This enhanced barrier effect not only minimized electrochemical attacks in static corrosion environments but also played a key role in reducing electrochemical degradation under frictional conditions.

Previous studies have demonstrated that Cr/CrN multilayer coatings exhibit superior corrosion resistance due to their dense and uniform structure, with performance strongly influenced by coating architecture, particularly total thickness and bilayer configuration [25–27]. However, a comprehensive understanding of the interplay between microstructural characteristics, electrochemical behavior, and nanomechanical properties remained incomplete. In particular, the evolution of the oxide film during corrosion and its impact on nanomechanical integrity have not been fully elucidated. Therefore, this study aims to bridge this gap by conducting an in-depth investigation into the microstructural, electrochemical, and nanomechanical properties of an optimized Cr/CrN multilayer coating exposed to a 3.5 % NaCl aqueous electrolyte. The multilayer system, composed of six Cr/CrN bilayers, was selected based on its demonstrated superiority in mechanical, tribological, and corrosion protective properties. A combination of advanced characterization techniques, including scanning electron microscopy and energy dispersive X-ray spectrometry (SEM-EDXS), atomic force microscopy (AFM), scanning Kelvin probe force microscopy (SKPFM), X-ray photoelectron spectroscopy (XPS), and AC/DC electrochemical analyses were employed to provide a comprehensive assessment of the coating microstructure, crystallographic orientation, surface morphology, local electronic properties, and corrosion behavior. Furthermore, the study focuses on the formation and evolution of the oxide film during corrosion, evaluating its role in passivation and its influence on the nanomechanical properties of the coating through nanoindentation. By systematically correlating these factors, this work aims to advance the fundamental understanding of Cr/CrN multilayer coatings upon exposure to corrosive environments and contribute to the optimization of protective coating strategies for industrial applications.

2. Experimental procedure

2.1. Materials

This study employed a Cr/CrN multilayer coating deposited onto 52100 bearing steel substrates via a physical vapor deposition (PVD) method [28]. The nominal steel composition (wt%) includes 0.98 %–1.10 % carbon, 1.30 %–1.60 % chromium, 0.15 %–0.30 % silicon, and 0.25 %–0.45 % manganese, with trace levels of sulfur (≤0.025 %) and phosphorus (≤0.025 %). The Cr/CrN multilayer consists of a Cr adhesion layer of ~ 200 nm followed by six Cr/CrN bilayers of period $\Lambda = 470$ nm, where the Cr has a thickness of ~50 nm and the CrN layer has a thickness of ~420 nm. The Cr and CrN layers have been deposited by PVD magnetron sputtering following proprietary recipes from SKF. The machined carbon steel substrates were thoroughly degreased using a heated alkaline solution. The arithmetic average roughness (Ra) of the carbon steel substrates prior to coating was measured to be 150 ± 30 nm using AFM (explained in 2.3). Surface cleanliness is critical for successful coating adhesion; therefore, in addition to washing and cleaning before the vacuum process, plasma etching was conducted inside the vacuum chamber. During the PVD deposition, a pure chromium (Cr) target served as the solid material source. For the Cr layers, the Cr target was sputtered with inert gasses, while for the CrN layers, a mixture of inert and nitrogen gas (N_2) in the chamber was used. Workpieces were mounted on rotating racks within the vacuum chamber to ensure uniform coating deposition, and the temperature of the process was kept below 170 °C to avoid damage to the steel substrates.

2.2. SEM and EDXS

The surface morphology and microstructure of the Cr/CrN coating were analyzed before and after corrosion testing using a scanning electron microscope (Teneo, FEI™) operated at 5 kV, 0.4 nA, and a working distance of 10 mm. Imaging was conducted with both secondary electron (SE) and backscatter electron (BSE) detectors, while an energy-dispersive X-ray spectroscopy (EDXS) detector was used for compositional analysis (operated at 20 kV, 1.6 nA, and a working distance of 10 mm).

2.3. AFM, and SKPFM

To investigate the surface topography and electronic surface potential evolution of the fresh Cr/CrN multilayer, atomic force microscopy (AFM) coupled with scanning Kelvin probe force microscopy (SKPFM) measurements were conducted. The experiments were performed using a Bruker Dimension Edge™ instrument equipped with an antimony (n)-doped silicon pyramid single crystal tip, coated with PtIr5 (SCM-Pit-V2 probe). The probe had a tip radius of 25 nm and a height of 10–15 μm. Surface potential maps were recorded in dual-scan mode. During the first scan, topography data were collected in dynamic mode (also known as tapping mode). In the second scan, the tip was lifted to 50 nm above the surface, and the surface potential was measured by following the topography contour registered in the initial scan. All topography and surface potential maps were acquired ex-situ in an air atmosphere at 22 °C and a relative humidity of approximately 40 %. The measurements employed a pixel resolution of 512 × 512, a zero DC bias voltage, and a scan frequency rate of 0.3 Hz. Histogram analysis, based on multimodal Gaussian distributions, was utilized to interpret the topography, amplitude, and surface potential distribution on the surface microstructure.

2.4. GIXRD

The Grazing-Incidence X-ray diffraction (GIXRD) measurements were performed using a Bruker D8 Discover diffractometer equipped with an Eulerian cradle and parallel beam geometry. On the incident beam side, a polycapillary optic (polycap) was used, providing a divergence of 0.25° with a beam size of 2 × 5 mm. The diffracted beam side was configured with a parallel Soller slit (0.35° divergence) and a graphite monochromator. The measurements were conducted using Co Kα radiation at an operating voltage of 45 kV and a current of 25 mA. Detector scans were performed in θ-2θ mode, covering the range of 10°–110° 2θ with a step size of 0.02° 2θ and a fixed θ angle of 5°. The counting time per step was set to 5 seconds. Data evaluation and analysis were carried out using Bruker DiffracSuite.EVA software (version 7.3).

2.5. XPS

X-ray photoelectron spectroscopy (XPS) was employed in this study to analyze the chemical states of the oxide layer on the Cr/CrN multilayer coating, both before and after exposure to the NaCl solution. The measurements were carried out using a PHI Versaprobe II spectrometer equipped with a monochromatic Al Kα X-ray source (1486.6 eV). The binding energy range was calibrated using Cu 2p3/2 (932.62 ± 0.1 eV) and Au 4f7/2 (83.96 ± 0.1 eV) reference peaks. Spectra were collected at a take-off angle of 45° with an X-ray beam diameter of 200 μm and an irradiation power of 49.6 W. The sample, a 25 × 10 × 4 mm 52100 steel plate coated with a Cr/CrN multilayer, was mounted on the specimen

holder using double-sided non-conductive tape. Charge neutralization was achieved using a combination of low-energy electrons and an Ar+ ion beam, calibrated against a PET reference sample. Minimal differential charging was observed, as evidenced by the absence of spectral tails in the C 1 s and O 1 s regions. Survey scans (1400–0 eV) were acquired using a pass energy of 187.5 eV, a step size of 1 eV, and 50 ms dwell time over 10 sweeps, revealing Cr, O, N, and C, with minor traces of Na. High-resolution scans of O 1 s, Cr 2p, N 1 s, and C 1 s were obtained with a pass energy of 23.5 eV, a step size of 0.1 eV, and 50 ms dwell time. Chamber pressure during measurement was ~7.5×10^{-9} Torr due to the Ar ion inflow required for charge neutralization. All spectra were charge-corrected relative to the C 1 s adventitious carbon peak (284.8 eV). Data analysis was performed using PHI Multipak software (version 9.9.2).

2.6. AC/DC electrochemical analyses

Electrochemical measurements were conducted using a three-electrode configuration with a Biologic SP-300 potentiostat. The Ag/AgCl/KCl (3 M) reference electrode (+222 mV vs. SHE), platinum mesh counter electrode, and Cr/CrN-coated working electrodes comprised the system. A 3.5 %wt NaCl electrolyte, prepared using ultra-pure Milli-Q water (resistivity >5 MΩ.cm) and J.T. Baker™ NaCl, was employed to simulate a corrosive environment. The electrolyte's pH was recorded as 5.6 at 22 ± 1°C. To stabilize the open-circuit potential (OCP), the samples were immersed in the solution for 1 hour prior to testing. Potentiodynamic polarization (PDP) was performed at a scan rate of 1 mV/s, beginning 100 mV below the OCP and extending to 1 V vs. Ag/AgCl. Electrochemical impedance spectroscopy (EIS) was conducted over a frequency range of 100 kHz to 10 mHz, applying a ± 10 mV sinusoidal perturbation after OCP analysis.

2.7. Nanomechanical analysis

Nanoindentation experiments were performed with a TI Premier Hysitron nanoindenter (Bruker, USA). The instrument has two load heads: the first one with a maximum load of 10 mN was used for studying low penetrations up to 350 nm depth, and the second one with a maximum load of 2 N was used to produce high penetrations up to 3300 nm. All tests were carried out using a Berkovich diamond indenter of 150 nm end-tip diameter in the load-controlled mode. The variation of the hardness and elastic modulus as a function of the indentation depth was realized by using a "load-partial-unload" (LPU) methodology which consisted of producing twenty loading/unloading cycles at

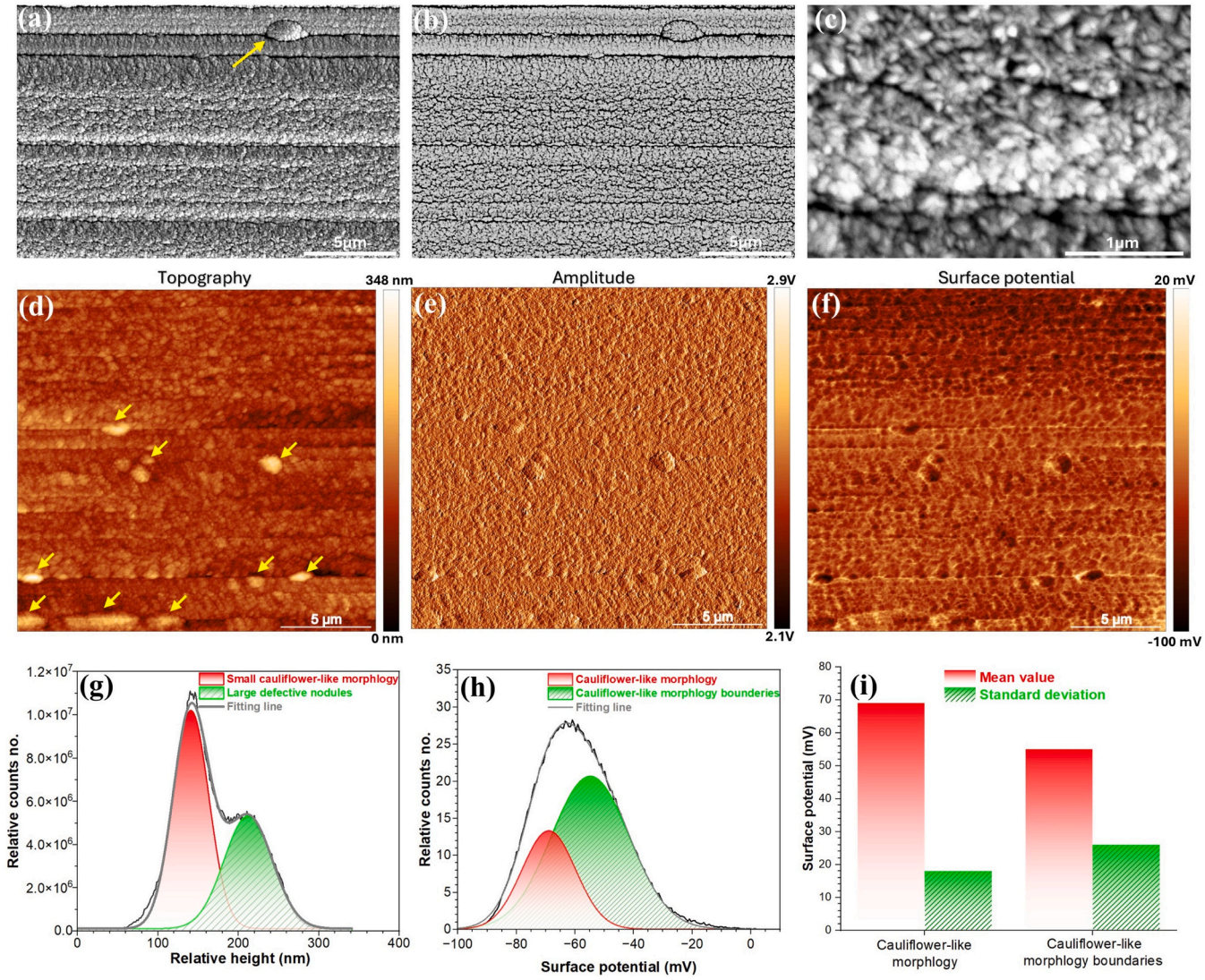

Fig. 1. (a–c) Top-view SEM images of the Cr/CrN multilayer coating at low and high magnifications, capturing both secondary (SE) and backscattered electron (BSE) signals, (d) Topography, (e) amplitude, and (f) electrical surface potential maps of the Cr/CrN coating, (g) Topography and (h) surface potential histograms obtained from d and f, respectively, (i) Mean value and standard deviation of surface potential extracted from h. The yellow arrows indicate nodular surface defects.

increasing target loads. All experiments were repeated at least 5 times, and the values of nanoindentation hardness (H_{IT}) and reduced elastic modulus (E_r) were calculated by the method of Oliver and Pharr [29].

3. Results and discussion

3.1. Morphological, microstructural, and electronic surface characteristics

Figs. 1**a and** 1**b** present the top-view SE and BSE-SEM images of the CrN top layer in the Cr/CrN multilayer coating. The surface morphology of the CrN top layer appears uniform, closely conforming to the underlying carbon steel substrate surface roughness. However, certain areas exhibit defects along the steel's machining trace lines (Figure S1), likely influenced by the substrate texture. In the high-magnification image presented in Fig. 1**c**, a uniform submicron cauliflower-like morphology is evident throughout the coating, distinctive of sputtering films deposited under low surface diffusion growth conditions [30]. Nevertheless, some regions exhibit nodular or granular surface defects ranging from 1 μm to 3 μm (indicated by the yellow arrows). These features are associated with the geometrical shadowing effect typical of PVD deposition techniques, where small seed particles expand during the coating process. The nodular defects specifically arise from foreign particles or droplets that settle on the substrate surface, either before or during the coating's growth phase [31].

The surface physical and electrical characteristics of the Cr/CrN multi-layer coating were evaluated through the generation of topography, amplitude, and electrical surface potential/charge maps, as depicted in Figs. 1**d, 1e, and** 1**f**. The combined topography and amplitude mappings provide a clear visualization of the small cauliflower-like structures and defective nodules (marked with yellow arrows on the topography map) on the CrN top layer. These small features are distinguished by slight differences in height and distribution, with a root mean square roughness (Rq) of 25 ± 6 nm. The height histogram from the topography image in Fig. 1**g** shows two distinct peaks: one for the small cauliflower-like morphology with mean heights of 140 nm and one at a height of 212 nm for the larger defective nodules. The highest surface potential and/or charge values are primarily associated with the cauliflower-like morphology, particularly at their nodule boundaries (Fig. 1**f**). Localized charges concentrated at grain or nodule boundaries can give rise to defect states, which in turn bend energy levels and establish a contact potential difference (ΔCPD) in the space charge regions adjacent to these boundaries [32,33]. As demonstrated in Fig. 1**h and** 1**i**, the surface potential histogram reveals a pseudo-heterogeneous distribution characterized by two deconvoluted peaks. Despite this heterogeneity, the Cr/CrN coating exhibits a defined surface potential range of −100–20 mV relative to PtIr, implying a weak tendency to form electrostatic interactions with the AFM tip apex [34]. This predominantly negative surface potential and/or charge distribution reflects a lower likelihood of electrochemical activity and reduced charge transfer and mass transport at the coating surface/electrolyte interface [35].

3.2. Crystalline microstructure, cross-sectional morphology, composition, and electronic properties

Fig. 2 displays the GIXRD pattern of a Cr/CrN multilayer coating on carbon steel, with overall fitting details provided in Figure S2. According to the GIXRD results (Fig. 2), the Cr/CrN multilayer coating exhibits distinct diffraction peaks at 43.8°, 51.1°, and 75.4°, corresponding to the CrN (111), CrN (200), and CrN (220) phases, based on PDF 04–007–9961. Additionally, weaker peaks observed at 91.6°, 96.3°, 119.9°, and 140.1° are associated with the CrN (311), CrN (222), CrN (400), and CrN (420) phases. The presence of nano Cr layers (~50 nm) is not evident in the GIXRD patterns, However, in the XRD patterns shown in Figure S2, the Cr diffraction peak at 44.4° exhibits significant intensity, corresponding to the Cr (110) phase, which is strongly

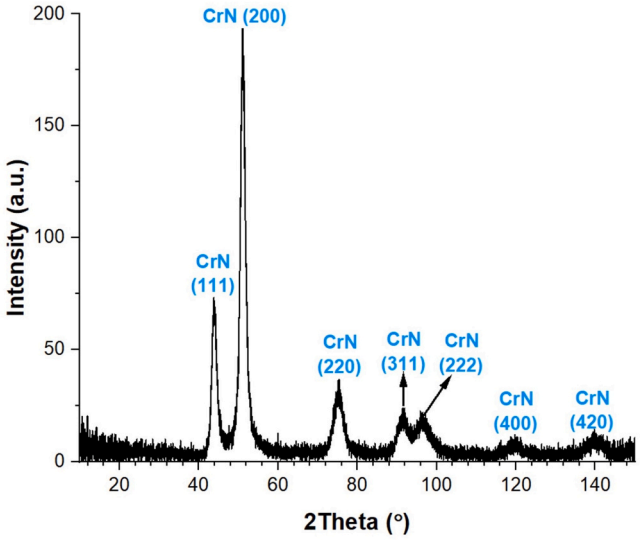

Fig. 2. GIXRD result of Cr/CrN coating applied on the carbon steel substrate.

influenced by the thick Cr adhesion layer. Smaller peaks at 65.1°, 82.1°, and 98.3° are attributed to Cr (200), Cr (211), and Cr (220), respectively, based on PDF 04–004–8467 for Cr. Overall, the preferential crystalline growth of CrN in the Cr/CrN multi-layer coating occurs along the [200] direction [36], which corresponds to the lowest surface energy [25].

Figs. 3**a and** 3**b** illustrate the BSE-SEM cross-sectional image and the merged multi-elemental map of the Cr/CrN multilayer coating applied to carbon steel. All these data were collected from a mirror-polished surface. The Cr/CrN multilayer coating exhibits a total thickness of 2.7 ± 0.4 μm (Fig. 3**a**), the exact thickness depending on the surface roughness and morphology of the underlying substrate. The visible individual layers include a Cr adhesion layer adjacent to the carbon steel, and alternating thin CrN and thin Cr layers, with thicknesses of approximately 250 nm, 420 nm, and 50 nm, respectively. There is no visible evidence of micro-cracks in the SEM/EDXS cross-sectional image of the polished surface, see Figs. 3**a and** 3**b**. However, the large-scale BSE-SEM images of the Cr/CrN multi-layer fracture surface (Fig. 3**c**) reveal a compact structure with some micro-cracks, alongside discontinuous columnar crystalline features [25,37]. The micro-cracks, highlighted by red arrows in Fig. 3**c**, appear perpendicular to the steel's machining trace lines (Figure S1) and are likely influenced by the substrate's roughness distribution (SEM images in Figs. 1**a and** 1**b**), contributing to the occurrence of defective sites. Surface roughness plays a crucial role in the corrosion performance of CrN PVD coatings. A rougher substrate promotes the preferential growth of columnar structures, increasing the likelihood of pinholes and microcracks, which can act as pathways for corrosive media, leading to localized corrosion and coating degradation [38]. In contrast, smoother substrates result in denser coatings with fewer defects, enhancing corrosion resistance. Studies have shown that coatings on smoother surfaces exhibit improved passivation behavior and lower corrosion rates, highlighting the correlation between surface finish, coating density, and corrosion performance [38–40]. Therefore, optimizing substrate roughness can significantly enhance the protective properties of CrN coatings.

Through cross-sectional analysis of the Cr/CrN multi-layer structure using SKPFM, the influence of both the composition and the electronic properties of individual layers (namely the Cr adhesion layer, CrN, and thin Cr layers) on the overall electronic surface potential was revealed. The conductive interface between layers results in Fermi-level alignment, driving electron migration from the lower work function (Φ) metal to the higher work function metal nitride [41,42]. Accordingly, cross-sectional electrical surface potential measurements may provide

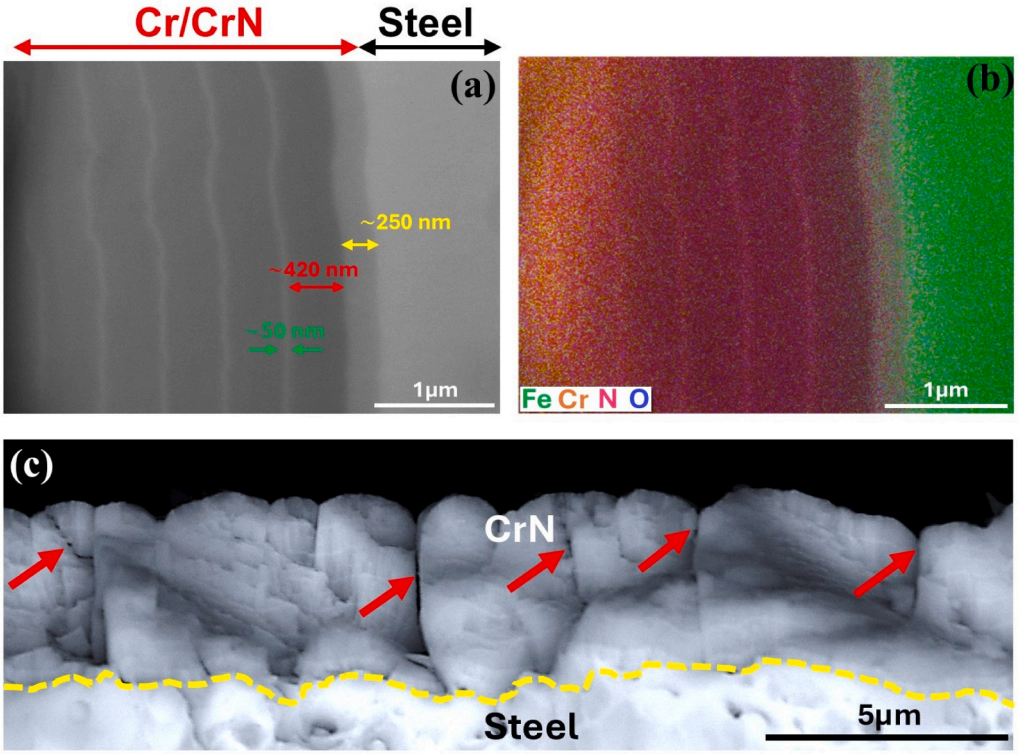

Fig. 3. (a) Cross-sectional BSE-SEM image of the Cr/CrN multilayer polished surface, (b) EDXS cross-sectional multi-elemental maps, and (c) Cross-sectional BSE-SEM image of the Cr/CrN multilayer fracture surface.

an indirect measure of the layers' intrinsic nobility [32]. Figs. 4**a,** 4**b and** 4**c** provide a detailed visualization of the topography, amplitude, and electrical surface potential of the Cr/CrN multi-layer coating after mirror polishing. The topography and amplitude profiles distinctly highlight the individual layers, with the Cr layers appearing lower in height than the CrN layers, reflecting their comparatively lower hardness value.

The SKPFM map presented in Fig. 4**c** reveals distinct electrical surface potential variations across the layers. The Cr adhesion layer exhibits the highest surface potential, followed by the Cr thin layers, and the CrN layers, which demonstrated the lowest surface potential. This aligns with previous studies, which indicate that the CrN layer exhibits a high work function of $\Phi_{CrN} = 5.1$ eV [43,44], exceeding that of Cr ($\Phi_{Cr} = 4.5$ eV) [45]. Additionally, this prior work demonstrated that the CrN layer has a lower surface potential compared to $SrTiO_{3-x}$, which, despite having a higher surface potential, possesses a lower work function ($\Phi_{SrTiO3-x} = 4.5$ eV) [43].

Analysis of the surface potential line profiles in Fig. 4**d** further quantifies these differences, showing a 5–10 mV potential difference between the CrN and Cr thin layers, and a more pronounced 60 mV difference between the CrN layer and the Cr adhesion layer. The surface potential histogram analysis derived from Fig. 4**e** vividly illustrates the electrical surface potential distribution across individual layers. Notably, a distinct surface potential signal is observed at the Cr adhesion layer/CrN interface. This phenomenon arises from charge accumulation in the space charge region and the reconfiguration of the energy diagram (energy band alignment) at this interface, which significantly influences the electrostatic force and the electronic surface potential [46,47].

When analyzing the correlation between corrosion studies and SKPFM data, variations in the work function among microstructural features and chemical compositions across different systems manifest as measurable differences in surface potential on the surface. These differences can reveal key electrochemical properties by identifying regions with varying levels of electrochemical activity and inherent nobility. However, the direct relationship between these surface potentials and actual corrosion behavior in real-world scenarios remains complex. Nevertheless, in this study at the Cr/CrN interface, differences in electrical surface potential point to variances in work function (e.g. Φ_{CrN} =5.1 eV and Φ_{Cr} = 4.5 eV), which, under localized corrosion conditions, foster micro-galvanic coupling. This accelerates the corrosion process, particularly at the Cr/CrN adhesion layer, where significant charge accumulation is observed.

3.3. *Surface chemical composition and complex oxide evolution*

The CrN top layer in the Cr/CrN multilayer coating develops a nanometer-thick oxide film, exhibiting various oxidation states when exposed to a 3.5 % NaCl solution, a highly aggressive environment. Hence, we conducted an analysis of the surface chemical composition and the evolution of various oxide states on the CrN top layer. This investigation was performed using XPS and encompassed both the fresh surface and the surface after 24 hours of exposure to a 3.5 % NaCl solution. Fig. 5 presents the high-resolution XPS spectra for Cr 2p, N 1 s, and O 1 s, before and after NaCl exposure. The Cr 2p spectra were fitted into multiple components, identifying metallic Cr^0 (574.1 eV), CrN (575.2 eV), and oxide and hydroxide of Cr (III) (576.69 eV, including Cr_2O_3 and $Cr(OH)_3$ [48,49]). The findings reveal that chromium predominantly existed in the CrN bonding state, accompanied by slight traces of oxide and hydroxide of Cr (III) (Fig. 5**d**) which aligns with prior research [48–50]. For the oxide/hydroxide, a single-component fit was chosen (Fig. 5**a**). It is recognized that this is an approximation and that for more accurate quantification of each individual oxide compound, an envelope fit of all the individual components is preferred (see [50]), but since the focus was on identifying whether the oxide layer grows upon corrosion, the single fit approximation was considered justified in this case. The presence of metallic Cr^0 may be attributed to the uneven distribution of the CrN top layer along the machining trace lines of the steel, which creates conditions that locally expose the topmost

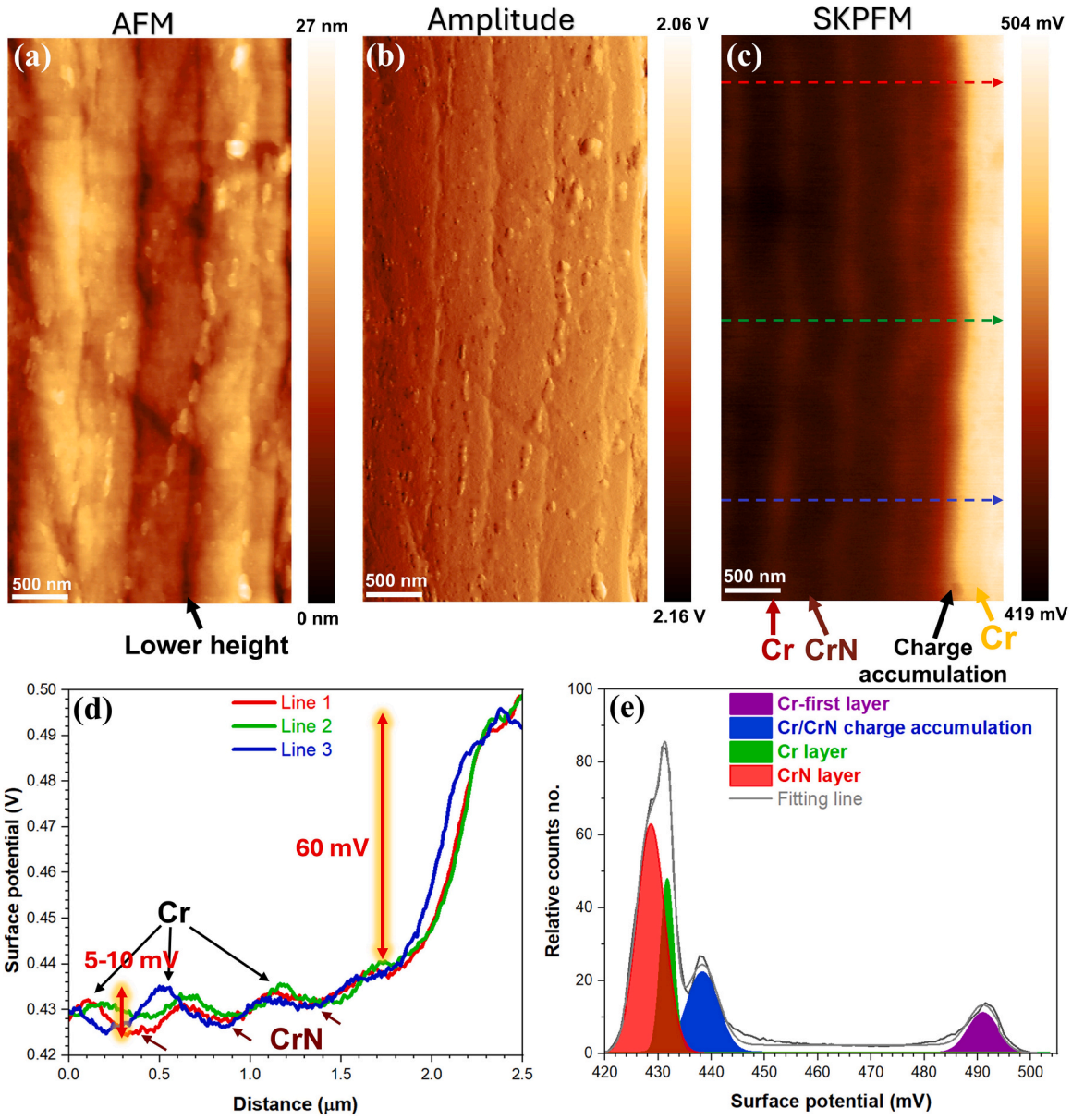

Fig. 4. (a-c) Cross-sectional topography, amplitude, and electrical surface potential maps of the Cr/CrN multi-layer polished coating, (d) surface potential line profiles obtained from c, (e) Surface potential histogram obtained from c.

underlying Cr thin layer at the surface. The N 1 s spectra (Fig. 5**b**) in the fresh surface condition were fitted with two components: one for CrN and one for chromium nitrites/nitrates (CrN_xO_y), with binding energies of 396.3 eV and 399.6 eV, respectively.

In the O 1 s spectrum (Fig. 5**c**), three characteristic peaks were identified, corresponding to lattice oxide (O^{2-}), hydroxide groups (OH^-), and adsorbed water molecules. With peak fitting binding energies were obtained at 529.9 eV, 531.6 eV, and 533.4 eV before exposure, and 529.8 eV, 531.3 eV, and 532.5 eV after exposure. When the CrN top layer was exposed to a 3.5 % NaCl solution for 24 h, an analysis of the elemental distribution (Fig. 5**e**) in the resulting complex oxide film showed an increase in oxygen content, while both chromium and nitrogen levels decreased. This can be attributed to the oxidation of the CrN surface, leading to the formation of chromium oxide and hydroxide species. This is consistent with the observed increase in the intensity peaks of overall chromium oxide and hydroxide species (Cr_2O_3 and $Cr(OH)_3$), along with a decrease in CrN peaks, as shown in the Cr 2p spectra (Fig. 5**a**) and the quantification results in Fig. 5**d**. Furthermore, in the O1s spectra, the intensity of the peak corresponding to O^{2-} is enhanced after exposure to 3.5 % NaCl, compared to the fresh surface condition. A notable observation is the presence of a chromium nitrites/nitrates (CrN_xO_y) peak under fresh surface conditions, which disappears after exposure to 3.5 % NaCl. The complex oxide film, formed on the CrN top layer, acts as a highly effective protective nanolayer [23]. Its exceptionally low degradation rate significantly hinders charge transfer and mass transport across the Cr/CrN oxide/electrolyte interfaces, as well as throughout the entire Cr/CrN multilayer system [48].

3.4. AC and DC electrochemical analyses

The electrochemical activity and corrosion resistance of the Cr/CrN multilayer coating were assessed during short-term exposure to a 3.5 wt % NaCl electrolyte, using open circuit potential (OCP), potentiodynamic polarization (PDP), and electrochemical impedance spectroscopy (EIS) techniques. The OCP evolution of the Cr/CrN multilayer coating in Fig. 6**a** exhibits a pronounced initial drop in corrosion potential, ranging from −15 mV to −233 mV vs. Ag/AgCl during the first 430 seconds of immersion in a 3.5 wt% NaCl solution. This is subsequently followed by

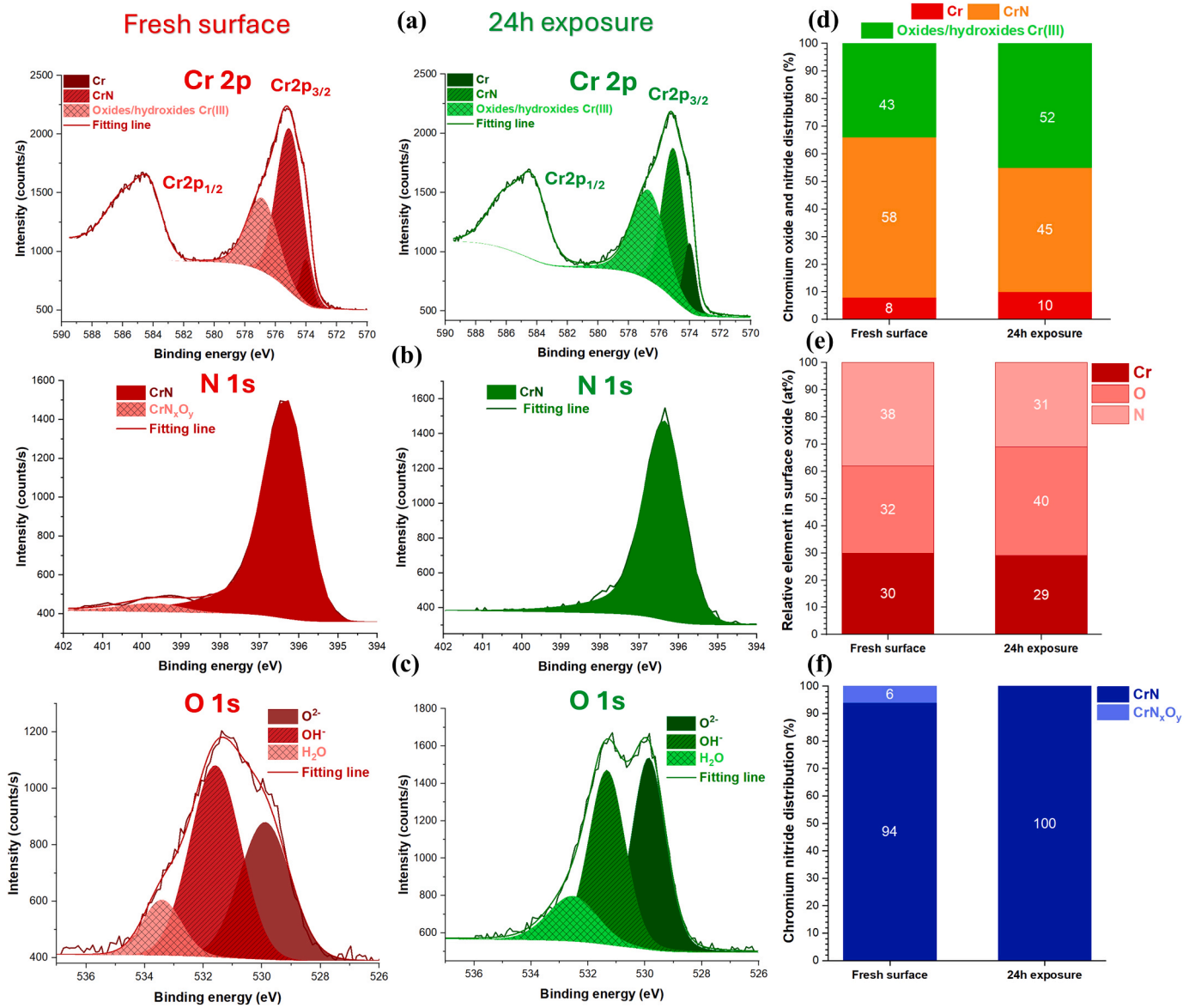

Fig. 5. XPS spectra of the (a) Cr 2p, (b) N1s, and (c) O 1 s electron energy regions on the Cr/CrN coating surface were obtained under two different conditions: fresh surface and after 24 h of free exposure to 3.5 wt% NaCl. The analysis includes (d) various oxidation states of chromium plus, (e) the surface oxide composition, and (f) various states of chromium nitrides. The peaks for H_2O and OH^- also include a minor contribution from oxygen bonded to organic carbon.

a significant stabilization, which is attributed to the dense, fine-grained microstructure of the coating and the low amount of surface defects, such as microcracks (which may be related to the steel machining trace lines) and pores [51,52]. This effect is particularly pronounced in the multi-layered arrangement of CrN and Cr layers. During the first 1 h of immersion, a gradual increase in corrosion potential was observed, stabilizing at −20 mV vs. Ag/AgCl. This change is attributed to surface oxidation processes, including the formation of chromium oxide and hydroxide (XPS 3.3) [7,12]. Notably, this represents a + 345 mV vs. Ag/AgCl difference compared to carbon steel.

Fig. 6**b** illustrates the PDP curves for both the Cr/CrN multilayer coating and carbon steel, recorded immediately after the EIS measurement. Using Tafel extrapolation, the corrosion current density (i_{corr}) and potential (E_{corr}) for both Cr/CrN multilayer coating and carbon steel were identified by locating the intersection points of tangents to the cathodic and anodic curves. By comparing both samples, it is clear that the Cr/CrN multilayer coating exhibits a notable reduction in corrosion current density, with a value of 0.27 μA.cm^{-2} for the Cr/CrN multilayer coating, compared to 5.9 μA.cm^{-2} for carbon steel. Additionally, the E_{corr} is significantly enhanced, with the Cr/CrN multilayer coating exhibiting E_{corr} = -245 mV vs. Ag/AgCl, in contrast to −563 mV vs. Ag/AgCl for carbon steel (Fig. 6**b**). Similarly, the Cr/CrN multilayer coating exhibits an activation region up to −88 mV vs. Ag/AgCl, after which a sudden breakdown occurs due to localized corrosion of the top CrN layer. Subsequently, multiple breakdown events are observed in the CrN layer, followed by minor passivation steps attributed to the thin Cr layers, as highlighted by the red arrows in the zoomed-in region of Fig. 6**c**. At an overpotential of approximately + 35 mV vs. Ag/AgCl, a stable passivation region becomes evident, extending up to + 850 mV vs. Ag/AgCl. This stability is attributed to the protective properties of the final thick Cr adhesion layer. Beyond + 850 mV vs. Ag/AgCl, pitting corrosion initiates in the thick Cr layer, leading to its breakdown and subsequent propagation into the underlying active carbon steel substrate (see the optical image of Cr/CrN multilayer coating after the PDP test is available in Figure S3). The coating breakdown is clearly demonstrated in the SE and BSE-SEM images, along with the EDXS maps shown in Fig. 7.

The EIS data for the Cr/CrN multilayer coating and carbon steel,

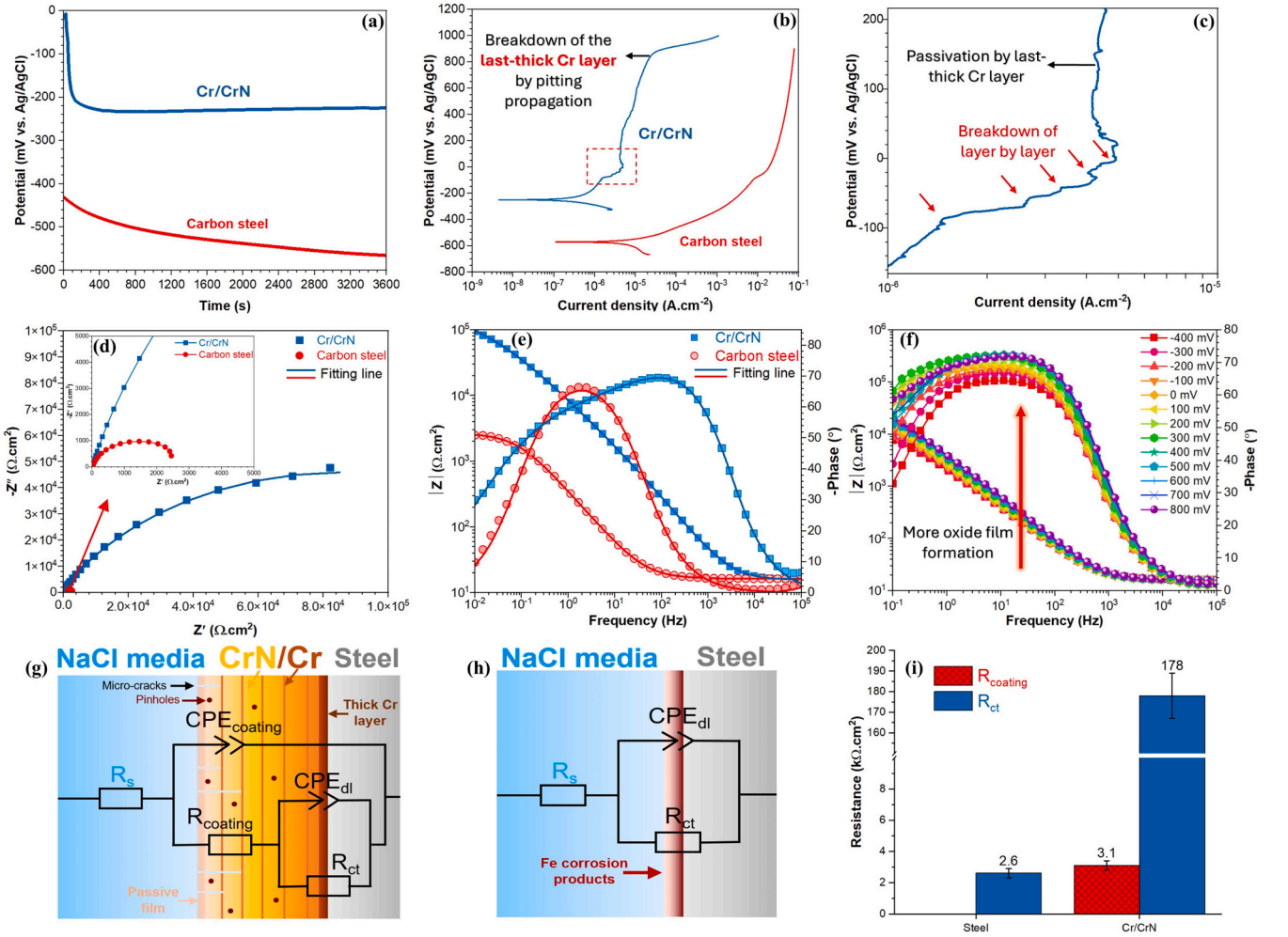

Fig. 6. (a) OCP and (b) PDP curves of the Cr/CrN multi-layer coating and carbon steel substrate during exposure to 3.5 wt% NaCl solution. (c) PDP magnified image from b indicating the breakdown of Cr/CrN multilayers and passivity region. (d) Nyquist plots, (e) Bode phase and amplitude plots for both Cr/CrN multilayer coating and carbon steel after 1 h of OCP monitoring in 3.5 wt% NaCl solution, (f) Dynamic EIS analysis (Bode phase and amplitude plots) of the Cr/CrN multilayer coating surface from −0.4 V to 0.8 V vs. Ag/AgCl after 1 hour of exposure to 3.5 wt% NaCl solution. The electrical equivalent circuit (EEC) model was used for fitting of the (g) Cr/CrN and (h) carbon steel EIS curves. (i) The resistance values for Cr/CrN coating and carbon steel were obtained from EIS fitting analysis.

depicted in Figs. 6**d and** 6**e**, demonstrate clear distinctions in corrosion behavior. The Nyquist plots show that the Cr/CrN multilayer coating achieves significantly greater real (Z′) and imaginary (-Z") impedance values, reflected by a notably larger semicircle diameter. This result confirms that the Cr/CrN multilayer coating exhibits a much higher charge transfer resistance, indicating exceptional corrosion protection when compared to carbon steel. The Bode phase diagram of the Cr/CrN multilayer coating, analyzed using the most appropriate equivalent electrical circuit (EEC), highlights the presence of two distinct time-constant elements in the parallel model (Fig. 6**g**) [10,52]. While, only one time constant was considered for the carbon steel substrate (Fig. 6**h**). The EEC is modelled with solution resistance (R_s), the resistance of Cr/CrN multilayer coating ($R_{coating}$), charge transfer resistance (R_{ct}), and constant phase elements including CPE $_{coating}$ and CPE $_{dl}$ corresponding to the coating and the double layer, respectively. The capacitance exhibits non-ideal behavior due to intrinsic material imperfections such as surface roughness, defects, and heterogeneities, which are appropriately represented by CPEs instead of ideal capacitors [53]. The CPE is described by the following equation:

$$Z_{CPE} = \frac{1}{Y_0 \quad (j\omega)^n} \tag{3}$$

Here, Y_0 represents the admittance of the CPE, j is the imaginary unit, ω denotes the angular frequency, and n is the CPE exponent. The value of n ranges between −1 and 1, where n = −1, n = 0, and n = 1 correspond to a system behaving as a pure inductor, pure resistor, and pure capacitor, respectively. The Bode phase and amplitude diagrams of the Cr/CrN multilayer coating show that the capacitance onset occurs at significantly higher frequencies compared to carbon steel (e.g. a delayed capacitive response occurs). This occurrence can be attributed to CrN's compact microstructure (fine grains and columnar microstructure) and the development of a complex chromium oxide film, which together demonstrate significant electronic characteristics (chromium oxides acting as a low charge-transfer semiconductor) and robust electrochemical stability [54]. The Cr_2O_3 and CrN exhibit work function values of $\Phi_{Cr2O3} = 5$ eV [55] and $\Phi_{CrN} = 5.1$ eV [43,44], respectively. These closely aligned work function values synergistically create a unique barrier to charge transfer and mass transport at the CrN/Cr_2O_3/electrolyte interfaces. Additionally, the exceptional properties described above are evident in dynamic-potential EIS (Fig. 6**f**), where an increase in overpotential causes both the Bode phase angle and magnitude to shift to higher values, indicating the evolution of surface oxidation or the formation of a complex chromium oxide film at the CrN/Cr_2O_3/electrolyte interfaces. The key EIS parameters, including capacitance and resistivity (Fig. 6**i**), were extracted for the Cr/CrN multilayer coating and carbon steel (all fitting parameters are available in Table S1).

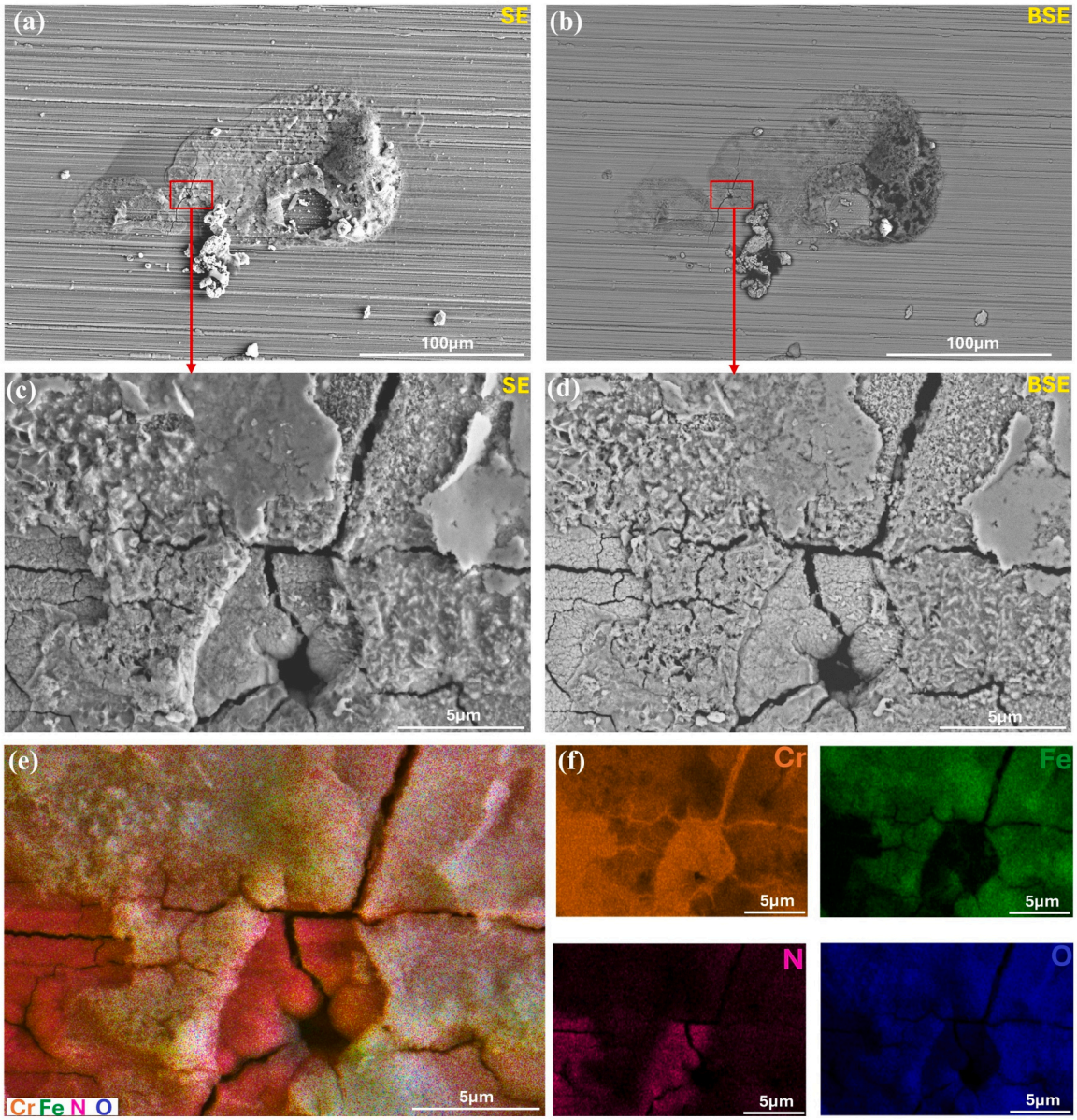

Fig. 7. (a) SE-SEM and (b) BSE-SEM images of the post-corroded Cr/CrN multilayer coating after PDP measurement until 1 V vs. Ag/AgCl, (c) SE-SEM and (d) BSE-SEM high magnification images from a and b, (e) Multi-color layer elemental map and (f) individual elemental maps of Cr/CrN multilayer coating indicating the fracture and/or pitting initiation region.

Overall, the Cr/CrN multilayer coating exhibits a higher double-layer capacitance (C_{dl} = ~72 µF.cm^{-2}) compared to the coating capacitance ($C_{coating}$ = ~10 µF.cm^{-2}). The extracted values for $R_{coating}$ and R_{ct} clearly indicate that the Cr/CrN multilayer coating-carbon steel interface shows significantly higher charge transfer resistance than the coating alone. This suggests the presence of surface defects, such as micro-cracks, pores, or pinholes, in the Cr/CrN multilayer coating's microstructure [27,56].

3.5. Long-term EIS monitoring of the electrochemical behavior and surface oxidation evolution

To gain deeper insights into the electrochemical activity and surface oxidation behavior of the Cr/CrN multi-layer coating, extended EIS monitoring was employed, as illustrated in Figs. 8**a and** 8**b**. The Nyquist diagram reveals that the semi-circle impedance values, represented by the real (Z′) and imaginary (-Z") components, exhibit a notable enhancement up to 5 hours. This trend aligns with the increasing Bode magnitude values, confirming the passivation process and the formation of a complex chromium oxide film with semiconductor characteristics (high work function (**SKPFM results in** Fig. 4)) on the CrN top layer (**XPS results in** 3.3). Similarly, the Bode phase angle values increase across the frequency range from 100 Hz to 0.01 Hz, further validating the formation of this protective film. Extracted $R_{coating}$ and R_{ct} values (Figs. 8**c and** 8**d,** all fitting parameters are available in Table S2) also show a marked rise up to 5 h, with R_{ct} peaking at 515 Ω.cm^2. After 5 hours of exposure, both the $R_{coating}$ and R_{ct} values decreased sharply, reaching their lowest levels within 24 hours. This trend is clearly evident in the reduction of the Nyquist semi-circle and the changes observed in the Bode phase and magnitude curves. XPS analyses after 24 h (Fig. 5) revealed a significant increase in the formation of complex chromium oxides (Cr_2O_3 and $Cr(OH)_3$), accompanied by a reduction in CrN. Despite the formation of protective oxides, the highly aggressive environment, coupled with increased availability of Cl^- ions and the presence of surface defects such as micro-cracks, trace lines, and pinholes, contributes to the localized corrosion process and overall decrease in

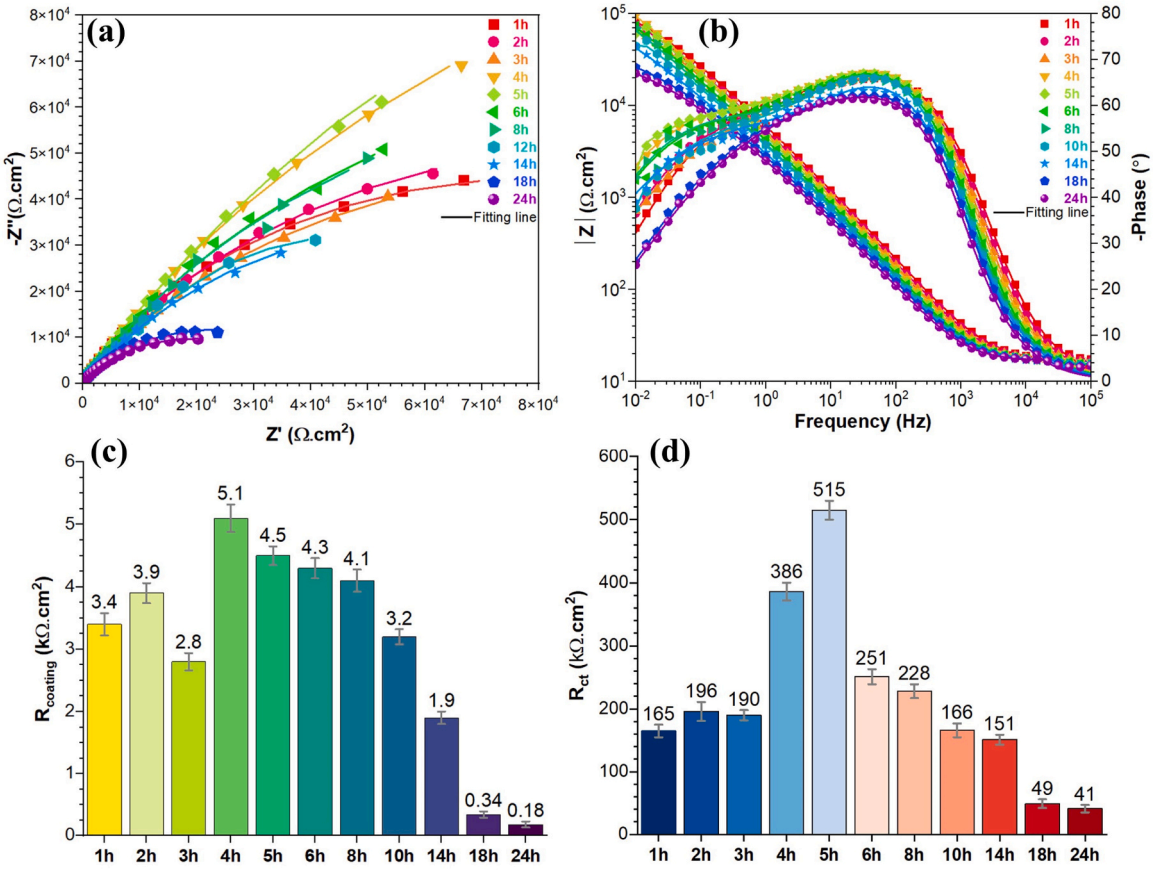

Fig. 8. (a) Nyquist and (b) Bode phase/amplitude monitoring plots for the Cr/CrN coating during 24 h of exposure in 3.5 wt% NaCl solution. (c) $R_{coating}$ and (d) R_{ct} values extracted from the fitting process of EIS curves in a and b.

resistivity.

3.6. *Nanomechanical properties of Cr/CrN multilayer coating after exposure to NaCl solution*

The hardness and elastic modulus of the Cr/CrN multilayer coating were calculated using the graphical method outlined in the ISO 14577 standard - Part 4 [57]. Figs. 9**a and** 9**b** display the LPU method used in the present experiments for maximum loads of 10 mN and 2 N, respectively. Figs. 9**c and** 9**d** illustrate representative Cr/CrN multilayer load-displacement curves obtained for both maximum loads.

By applying the LPU with a maximum load of 2 N (Fig. 9**b**), load-displacement curves for hardness (H_{IT}) and reduced elastic modulus (E_r) as a function of penetration depth (h) were obtained, as shown in Figs. 10**a and** 10**b**, respectively. The H_{IT} increases until it reaches a maximum at approximately 200 nm penetration, then decreases to a value of ~9.2 GPa at a penetration of ~3300 nm. According to ISO 14577, the maximum value corresponds to the coating hardness, which is found to be $H_{IT} = 14.86 \pm 0.32$ GPa. The hardness value at maximum penetration is very close to the steel hardness, $H_{IT} = 8.98 \pm 0.97$ GPa [58], as indicated by the black dashed line in Fig. 10**a**. The E_r exhibits a similar trend (Fig. 10**b**), increasing until a penetration depth of approximately 180 nm, and then decreasing to a value of ~193 GPa at ~3300 nm. The maximum in the curve corresponds to the Cr/CrN multilayer coating's reduced elastic modulus, $E_r = 213.4 \pm 1.1$ GPa, and the value at maximum penetration is close to the reported value for the steel substrate, $E_r = 197.6 \pm 8.4$ GPa [58], which is also indicated by the black dashed line in Fig. 10**b**. Several studies have reported on the nanomechanical properties of Cr/CrN multilayers (see [59] and references therein). It has been observed that the hardness and elastic modulus of these multilayers are influenced by the bilayer period, total coating thickness, and the PVD deposition conditions. The mechanical behavior, as a function of penetration depth, along with the coating's H_{IT} and E_r values, are consistent with those reported by Shan et al. [59].

Corrosion is well-documented to degrade the mechanical properties of materials [60]. Nanoindentation offers precise control over indentation depth, ranging from nanometers to microns, enabling the measurement of H_{IT} and E_r values of surface physicochemical events, especially corrosion and passivation. Using this technique, we directly correlate the weakening of surface nanomechanical properties caused by complex oxide formation (a positive effect in corrosion performance) and the detrimental physicochemical surface evolutions (as a weak point) with EIS (Fig. 8) and XPS (Fig. 5) results after 24 hours of exposure to 3.5 % NaCl. To investigate these effects, the nanomechanical properties of a CrN surface coating before and after 24 h of immersion in 3.5 % NaCl were measured using a low-load sensor head of the nanoindenter. This setup also facilitated surface imaging by employing surface probe microscopy (SPM) mode with a Berkovich diamond tip. Initially, the sample surfaces were imaged, and indentation points were carefully selected on flat regions of the CrN top layer to minimize the influence of steel's polishing trace lines on H_{IT} and E_r measurements [29]. All measurements were conducted using the LPU method, as shown in Fig. 9**a.** The top surface of the Cr/CrN multilayer coating was analyzed in two samples: the sample exposed to 3.5 % NaCl and the fresh, unexposed surface. Figs. 11**a and** 11**c**, along with Figs. 11**b and** 11**d**, show the SPM topography and gradient images obtained after experiments on these regions, respectively. Residual indentations were clearly observed on the CrN top-layer surface. The H_{IT} and E_r results are presented in Figs. 11**e and** 11**f**, respectively. At the exposed surface after 24 hours in 3.5 % NaCl solution, the surface exhibited softening, with

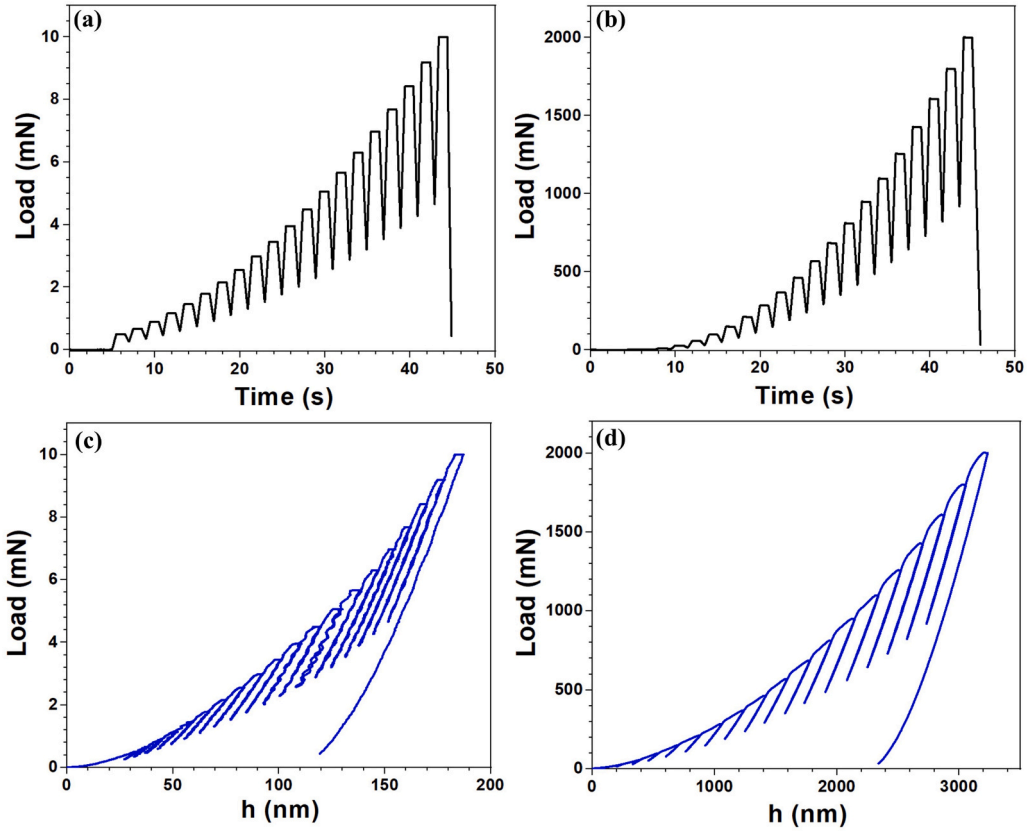

Fig. 9. Multiple partial loading/unloading nanoindentations methodologies were used in the present experiments for maximum loads of (a) 10 mN and (b) 2 N. Representative load-displacement curves for Cr/CrN multilayer coatings were obtained for maximum loads of (c) 10 mN and (d) 2 N.

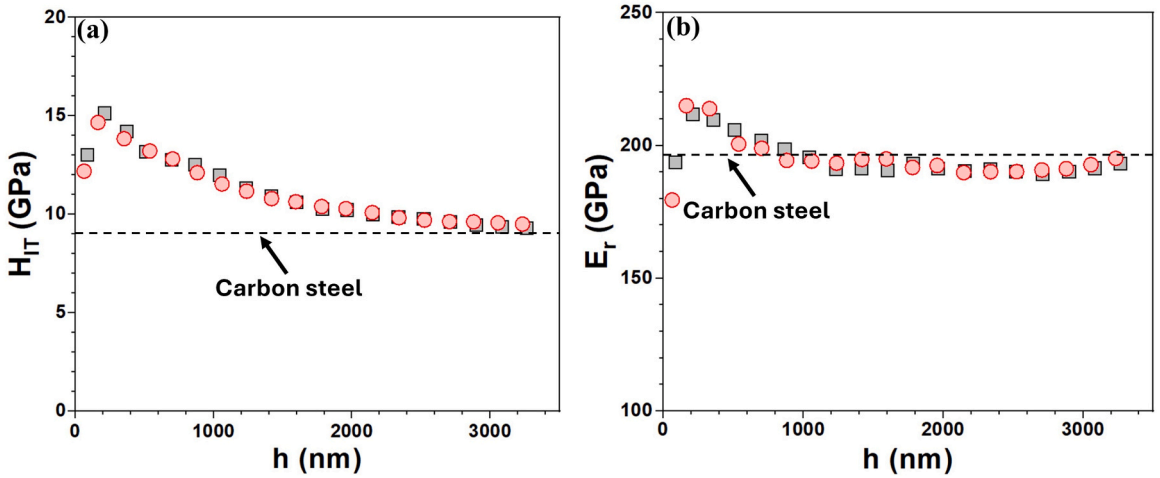

Fig. 10. Mechanical properties of the Cr/CrN multilayer coating vs penetration depth measured by the LPU method displayed in Fig. 9b: (a) hardness and (b) reduced elastic modulus. Each color corresponds to a different measurement. The dashed lines correspond to the steel substrate values taken from the reference [58].

H_{IT} values ranging from 6–13 GPa and E_r from 130–180 GPa at penetration depths of 40–200 nm. In contrast, the fresh surface displayed higher hardness, with H_{IT} values between 11–15 GPa and E_r from 185–215 GPa at penetrations of 30–200 nm. These results align well with the XPS data, which indicate the formation of a more complex chromium oxide film with reduced hardness compared to CrN. Moreover, the physicochemical degradation, encompassing alterations in surface morphology and the failure process within the Cr/CrN multilayer, notably diminished the hardness, elastic modulus, and electrochemical resistivity of the Cr/CrN coating.

4. Physicochemical surface evolution effects on nanomechanical and corrosion protective properties

The Cr/CrN multilayer coating performance in corrosive environments is governed by the complex physicochemical interactions between its structural integrity, electrochemical stability, and nanomechanical properties. Based on the XPS and EIS results, after 24 h of exposure to a 3.5 % NaCl solution, significant changes were observed, beginning with the surface oxidation of the CrN top layer. high resolution XPS and corresponding surface elemental distribution analysis

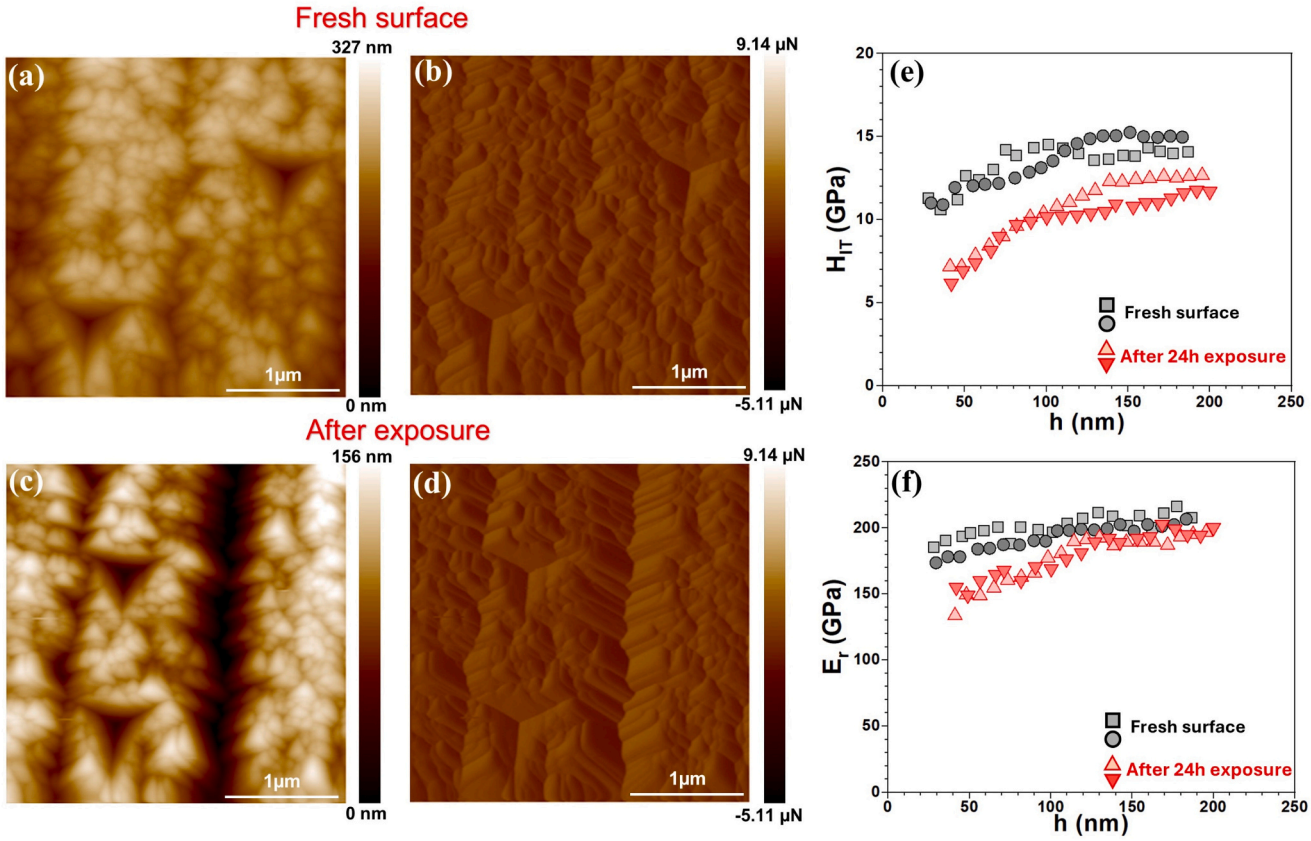

Fig. 11. (a,c) SPM topography and (b,d) gradient images of the CrN surface layer after two sets of experiments done on individual regions including a fresh coating surface and a coating surface exposed to 3.5 % NaCl for 24 h. The resulting H_{IT} and E_r from these measurements are shown in (e) and (f), respectively.

(Figs. 5**c and** 5**e**) revealed an increase in oxygen content, along with changes in the distribution of oxygen species (HO^- and O^{2-}), while chromium and nitrogen levels decreased, indicating the formation of a chromium oxide (Cr_2O_3) and hydroxide ($Cr(OH)_3$) film. XPS data (Fig. 5**a**) confirmed this transformation, with increased Cr oxide peaks and a reduction in CrN, which initially enhances corrosion resistance by reducing the penetration of aggressive ions.

However, surface defects such as micro-cracks, identified in the BSE-SEM fracture images (Fig. 3**c**), serve as pathways for chloride ions to penetrate the Cr/CrN multilayer coating. This localized corrosion is evident in the electrochemical results from EIS (Fig. 8), where a decrease in both the $R_{coating}$ and R_{ct} values indicates enhanced corrosion at these defect sites. The progressive corrosion weakens the protective chromium oxide layer, leading to a decline in the coating ability to resist further degradation. In parallel, nanoindentation tests (Fig. 11) reveal a reduction in hardness (H_{IT}) and elasticity (E_r) after 24 h of exposure to a 3.5 % NaCl solution, correlating with the formation of a mechanically weaker chromium oxide layer. The combined mechanical degradation and corrosion at defect sites lead to a substantial reduction in both the electrochemical stability and mechanical integrity of the coating.

Thus, while the chromium oxide film initially provides protection, surface imperfections, such as micro-cracks, accelerate localized corrosion and compromise the coating durability. This highlights the critical importance of minimizing surface defects to enhance the long-term performance of Cr/CrN coatings in aggressive environments. A schematic representation (Fig. 12) further illustrates how the Cr/CrN coating's compact microstructure, characterized by fine grains, a fragmented columnar crystalline structure, and a low number of micro-cracks, undergoes concurrent physicochemical modifications, ultimately driving its gradual corrosion protection degradation. The

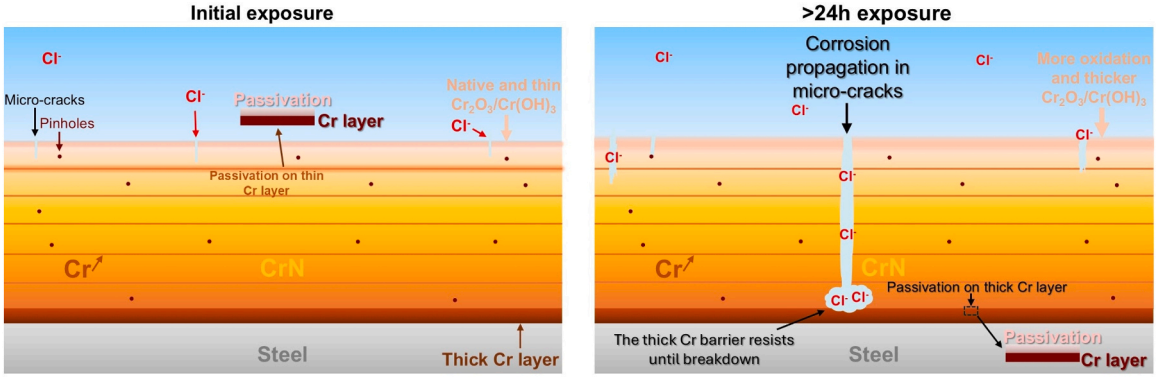

Fig. 12. Schematic illustration of the progressive corrosion process in an optimized Cr/CrN multilayer coating.

significant decline in impedance value observed in the Cr/CrN multilayer coating when exposed to a 3.5 % NaCl solution (**EIS in** Fig. 8) is primarily attributed to localized corrosion triggered by the aggressive penetration of Cl^- ions into surface defects such as micro-cracks, pinholes, and other structural irregularities. These imperfections act as channels, allowing Cl^- ions to infiltrate deeper layers, initiating and propagating corrosion degradation. As corrosion advances, it undermines the protective properties of the multilayer coating, particularly the passivation provided by the Cr thin-layer (~50 nm). Over time, this continuous attack compromises the coating's structural integrity and durability, leaving it increasingly vulnerable to failure in harsh environments.

5. Conclusions

This research presents a thorough and systematic investigation into the microstructure, corrosion mechanisms, and nanomechanical properties of an optimized Cr/CrN multilayer coating in a 3.5 % NaCl solution. By employing a variety of advanced techniques, including SEM-EDXS, AFM, SKPFM, XPS, and AC/DC multielectrochemical analyses, we uncovered detailed insights into the coating's microstructure, crystallographic orientations, morphology, local surface electronic properties, and electrochemical behavior. The key findings are summarized below:

1. The coating exhibits a uniform submicron cauliflower-like structure, with localized defects such as nodular or granular features (1–3 μm) and steel's polishing trace lines. These defects result from geometrical shadowing effects inherent to PVD techniques, influenced by foreign particles and surface roughness of the substrate during deposition.
2. The CrN coating displays subtle surface roughness variations (Rq = 25 ± 11 nm) with distinct morphologies, including smaller cauliflower-like features (~140 nm) and larger nodules (~212 nm). Localized charges at boundaries create defect states and a predominantly negative surface potential (-100–20 mV), suggesting low electrochemical activity and limited charge transfer.
3. The surface potential analysis shows a 5–10 mV difference between CrN and Cr layers, and a 60 mV difference at the Cr/CrN adhesion interface. These potential variations, due to differences in work function (Φ_{CrN} = 5.1 eV, Φ_{Cr} = 4.5 eV), promote micro-galvanic coupling, accelerating corrosion, especially at the interface of the CrN and Cr adhesion layer where charge accumulation occurs.
4. The protective complex oxide film formation upon exposure to a 3.5 % NaCl solution is supported by increasing Bode phase angle values and rising $R_{coating}$ and R_{ct} values up to 5 hours, with R_{ct} peaking at 515 $\Omega.cm^2$. After 5 h, both values decrease, as seen in Nyquist and Bode curve changes. XPS analysis shows increased chromium oxide formation (Cr_2O_3, $Cr(OH)_3$) and reduced metallic Cr and CrN.
5. Overall, the significant decrease in the total impedance of the Cr/CrN multilayer in 3.5 % NaCl solution is attributed to localized corrosion caused by aggressive Cl^- ions penetrating surface defects, such as micro-cracks, which facilitate corrosion propagation and accelerate the degradation process.
6. The significant reductions in hardness (H_{IT}) and elastic modulus (E_r) close to the surface confirm that the CrN top layer undergoes notable physicochemical degradation after prolonged exposure (24 h) to a 3.5 % NaCl solution. The formation of a chromium oxide film with lower mechanical properties further emphasizes the impact of corrosion-induced softening and reduced protective mechanical performance.

CRediT authorship contribution statement

Mol Arjan: Writing – review & editing, Visualization, Validation, Supervision, Resources, Project administration, Funding acquisition, Conceptualization. **Nijdam Thijs:** Writing – review & editing, Investigation, Formal analysis, Data curation. **Rahimi Ehsan:** Writing – review & editing, Writing – original draft, Validation, Methodology, Investigation, Formal analysis, Data curation, Conceptualization. **Broitman Esteban:** Writing – review & editing, Validation, Supervision, Project administration, Methodology, Investigation, Formal analysis, Data curation, Conceptualization. **Jahagirdar Adwait:** Writing – review & editing, Data curation.

Contribution

E. Rahimi conceived the idea and guided the project. T. Nijdam performed the XPS characterization and assisted with the interpretation of the XPS results. E. Broitman accomplished the nanomechanical characterization and the following discussion. A. Jahagirdar supported and prepared all coating samples. Both E. Broitman and A. Mol supervised the project, discussed the results, and revised the manuscript. All authors wrote the manuscript and contributed to the overall scientific interpretation

Author Agreement Statement

We the undersigned declare that this manuscript is original, has not been published before and is not currently being considered for publication elsewhere. We confirm that the manuscript has been read and approved by all named authors and that there are no other persons who satisfied the criteria for authorship but are not listed. We further confirm that the order of authors listed in the manuscript has been approved by all of us.

Declaration of Competing Interest

The authors declare that they have no known competing financial interests or personal relationships that could have appeared to influence the work reported in this paper.

Acknowledgments

This research was carried out under project number T23011 in the framework of the Research Program of the Materials Innovation Institute (M2i) (www.m2i.nl), and was funded by Holland High Tech | TKI HSTM via the PPS allowance scheme for public-private partnerships. E. Rahimi and A.Mol also thank the SKF company for providing funding and allowing the use of their research facilities.

Appendix A. Supporting information

Supplementary data associated with this article can be found in the online version at doi:10.1016/j.corsci.2025.112943.

Data availability

Data will be made available on request.

References

[1] J. Wu, W. Wang, M. Shen, S. Zhu, A comparative study of the electrochemical corrosion behavior between Cr2N and CrN coatings, Heat. Treat. Surf. Eng. 4 (2022) 64–69.
[2] Z. Li, C. Liu, Q. Chen, J. Yang, J. Liu, H. Yang, W. Zhang, R. Zhang, L. He, J. Long, H. Chang, Microstructure, high-temperature corrosion and steam oxidation properties of Cr/CrN multilayer coatings prepared by magnetron sputtering, Corros. Sci. 191 (2021) 109755.
[3] A. Gilewicz, P. Chmielewska, D. Murzynski, E. Dobruchowska, B. Warcholinski, Corrosion resistance of CrN and CrCN/CrN coatings deposited using cathodic arc evaporation in Ringer's and Hank's solutions, Surf. Coat. Technol. 299 (2016) 7–14.

[4] B. Biswas, Y. Purandare, A. Sugumaran, I. Khan, P.E. Hovsepian, Effect of chamber pressure on defect generation and their influence on corrosion and tribological properties of HIPIMS deposited CrN/NbN coatings, Surf. Coat. Technol. 336 (2018) 84–91.

[5] R. Akhter, Z. Zhou, Z. Xie, P. Munroe, Harmonizing mechanical responses of nanostructured CrN coatings via Ni additions, Appl. Surf. Sci. 538 (2021) 147987.

[6] Y. Wang, J. Zhang, S. Zhou, Y. Wang, C. Wang, Y. Wang, Y. Sui, J. Lan, Q. Xue, Improvement in the tribocorrosion performance of CrCN coating by multilayered design for marine protective application, Appl. Surf. Sci. 528 (2020) 147061.

[7] J. Zhang, Z. Li, Y. Wang, S. Zhou, Y. Wang, Z. Zeng, J. Li, A new method to improve the tribological performance of metal nitride coating: A case study for CrN coating, Vacuum 173 (2020) 109158.

[8] S.K. Pradhan, C. Nouveau, A. Vasin, M.A. Djouadi, Deposition of CrN coatings by PVD methods for mechanical application, Surf. Coat. Technol. 200 (2005) 141–145.

[9] A. Kafizas, C.J. Carmalt, I.P. Parkin, CVD and precursor chemistry of transition metal nitrides, Coord. Chem. Rev. 257 (2013) 2073–2119.

[10] J.-Z. Kong, C. Li, X.-Y. Sun, Y. Xuan, H.-F. Zhai, A.-D. Li, Q.-Z. Wang, F. Zhou, Improved tribological properties and corrosion protection of CrN coating by ultrathin composite oxide interlayer, Appl. Surf. Sci. 541 (2021) 148606.

[11] G. Biava, I.Bd.A.F. Siqueira, R.F. Vaz, G.B. de Souza, H.C.M. Jambo, A. Szogyenyi, A.G. Pukasiewicz, Evaluation of high temperature corrosion resistance of CrN, AlCrN, and TiAlN arc evaporation PVD coatings deposited on Waspaloy, Surf. Coat. Technol. 438 (2022) 128398.

[12] L. Shan, Y. Wang, Y. Zhang, Q. Zhang, Q. Xue, Tribocorrosion behaviors of PVD CrN coated stainless steel in seawater, Wear 362 (2016) 97–104.

[13] S. Zhou, V. Pelenovich, B. Han, M. Yousaf, S. Yan, C. Tian, D. Fu, Effects of modulation period on microstructure, mechanical properties of TiBN/TiN nanomultilayered films deposited by multi arc ion plating, Vacuum 126 (2016) 34–40.

[14] N.E. Beliardouh, K. Bouzid, C. Nouveau, B. Tlili, M.J. Walock, Tribological and electrochemical performances of Cr/CrN and Cr/CrN/CrAlN multilayer coatings deposited by RF magnetron sputtering, Tribology Int. 82 (2015) 443–452.

[15] D. Wang, M. Hu, X. Gao, D. Jiang, Y. Fu, L. Weng, J. Sun, Tailoring of the interface morphology of WS2/CrN bilayered thin film for enhanced tribological property, Vacuum 156 (2018) 157–164.

[16] Y. Vengesa, A. Fattah-alhosseini, H. Elmkhah, O. Imantalab, M.K. Keshavarz, Investigation of corrosion and tribological characteristics of annealed CrN/CrAlN coatings deposited by CAE-PVD, Ceram. Int. 49 (2023) 3016–3029.

[17] T. Rajabi, M. Atapour, H. Elmkhah, S.M. Nahvi, Nanometric CrN/CrAlN and CrN/ZrN multilayer physical vapor deposited coatings on 316L stainless steel as bipolar plate for proton exchange membrane fuel cells, Thin Solid Films 753 (2022) 139288.

[18] Y. Purandare, G. Robinson, A. Ehiasarian, P.E. Hovsepian, Investigation of High Power Impulse Magnetron Sputtering deposited nanoscale CrN/NbN multilayer coating for tribocorrosion resistance, Wear 452 (2020) 203312.

[19] L. Wang, M. Wang, H. Chen, Corrosion mechanism investigation of TiAlN/CrN superlattice coating by multi-arc ion plating in 3.5 wt% NaCl solution, Surf. Coat. Technol. 391 (2020) 125660.

[20] M. Beltrami, A. Mavrič, S. Dal Zilio, M. Fanetti, G. Kapun, M. Lazzarino, O. Sbaizero, M. Čekada, A comparative study of nanolaminate CrN/Mo2N and CrN/W2N as hard and corrosion resistant coatings, Surface and Coatings Technology 455 (2023) 129209.

[21] Y.X. Ou, J. Lin, H.L. Che, W.D. Sproul, J.J. Moore, M.K. Lei, Mechanical and tribological properties of CrN/TiN multilayer coatings deposited by pulsed dc magnetron sputtering, Surf. Coat. Technol. 276 (2015) 152–159.

[22] L. Liao, Q. Wan, H. Wang, B. Yang, Q. Mei, Irradiation enhanced corrosion resistance of CrN/TiSiN multilayers synthesized by cathodic arc ion plating, Mater. Today Commun. 35 (2023) 106155.

[23] S. Kaciulis, A. Mezzi, G. Montesperelli, F. Lamastra, M. Rapone, F. Casadei, T. Valente, G. Gusmano, Multi-technique study of corrosion resistant CrN/Cr/CrN and CrN: C coatings, Surf. Coat. Technol. 201 (2006) 313–319.

[24] Y. Chipatecua, J. Olaya, D.F. Arias, Corrosion behaviour of CrN/Cr multilayers on stainless steel deposited by unbalanced magnetron sputtering, Vacuum 86 (2012) 1393–1401.

[25] Y. Wang, J. Zhang, Y. Wang, C. Wang, W. Guo, X. Lu, Y. Sui, J. Lan, Inhibiting tribocorrosion damage of Cr/CrxN coatings by multi-layer design, Ceram. Int. 47 (2021) 842–850.

[26] J. He, X. Lan, Z. Liu, D. Jiao, X. Zhong, Y. Cheng, C. Tang, W. Qiu, Modification of Cr/CrN composite structure by Fe addition and its effect on decorative performance and corrosion resistance, Ceram. Int. 47 (2021) 23888–23894.

[27] R. Bayón, A. Igartua, X. Fernández, R. Martínez, R. Rodríguez, J.A. García, A. De Frutos, M. Arenas, J. De Damborenea, Corrosion-wear behaviour of PVD Cr/CrN multilayer coatings for gear applications, Tribology Int. 42 (2009) 591–599.

[28] SKF Coatings, in: S. Group (Ed.), 2020. https://cdn.skfmediahub.skf.com/api/public/0901d19680a4e17f/pdf_preview_medium/0901d19680a4e17f_pdf_preview_medium.pdf.

[29] E. Broitman, Indentation hardness measurements at macro-, micro-, and nanoscale: a critical overview, Tribology Lett. 65 (2017) 23.

[30] J.A. Thornton, High rate thick film growth, Annu. Rev. Mater. Sci. 7 (1977) 239–260.

[31] P. Panjan, P. Gselman, M. Panjan, T. Bončina, A. Drnovšek, M. Albu, M. Čekada, F. Zupanič, Microstructure and Surface Topography Study of Nanolayered TiAlN/CrN Hard Coating, Coatings 12 (2022) 1725.

[32] M. Mousavi, E. Rahimi, J.M.C. Mol, Y. Gonzalez-Garcia, The effect of phosphorous content on the microstructure and localised corrosion of electroless nickel-coated copper, Surf. Coat. Technol. 492 (2024) 131174.

[33] T.-X. Qin, E.-M. You, M.-X. Zhang, P. Zheng, X.-F. Huang, S.-Y. Ding, B.-W. Mao, Z.-Q. Tian, Quantification of electron accumulation at grain boundaries in perovskite polycrystalline films by correlative infrared-spectroscopic nanoimaging and Kelvin probe force microscopy, Light.: Sci. Appl. 10 (2021) 84.

[34] E. Rahimi, A. Imani, M. Lekka, F. Andreatta, Y. Gonzalez-Garcia, J.M.C. Mol, E. Asselin, L. Fedrizzi, Morphological and Surface Potential Characterization of Protein Nanobiofilm Formation on Magnesium Alloy Oxide: Their Role in Biodegradation, Langmuir 38 (2022) 10854–10866.

[35] E. Rahimi, D. Kim, R. Offoiach, R. Sanchis-Gual, X.-Z. Chen, P. Taheri, Y. Gonzalez-Garcia, J.M.C. Mol, L. Fedrizzi, S. Pané, M. Lekka, Biodegradation of Oxide Nanoparticles in Apoferritin Protein Media: A Systematic Electrochemical Approach, Adv. Mater. Interfaces 10 (2023) 2300558.

[36] F. Jasempoor, H. Elmkhah, O. Imantalab, A. Fattah-Alhosseini, Comparison of electrochemical behavior of CrN single-layer coating and Cr/CrN nanolayered coating produced by cathodic arc evaporation physical vapor deposition, Int. J. Appl. Ceram. Technol. 19 (2022) 2222–2235.

[37] D. Wang, M. Hu, D. Jiang, Y. Fu, Q. Wang, J. Yang, J. Sun, L. Weng, The improved corrosion resistance of sputtered CrN thin films with Cr-ion bombardment layer by layer, Vacuum 143 (2017) 329–335.

[38] S.-C. Lee, W.-Y. Ho, F. Lai, Effect of substrate surface roughness on the characteristics of CrN hard film, Mater. Chem. Phys. 43 (1996) 266–273.

[39] J.-F. Tang, C.-H. Huang, C.-Y. Lin, Y.-J. Tsai, C.-L. Chang, Effect of plasma nitriding and modulation structure on the adhesion and corrosion resistance of CrN/Cr2O3 coatings, Surf. Coat. Technol. 379 (2019) 125051.

[40] P. Wongpanya, S. Tunmee, C. Euaruksakul, P. Songsiriritthigul, N. Witit-Anun, Corrosion behaviors and mechanical properties of CrN film, Adv. Mater. Res. 853 (2014) 155–163.

[41] E. Rahimi, A. Rafsanjani-Abbasi, A. Imani, S. Hosseinpour, A. Davoodi, Insights into Galvanic Corrosion Behavior of Ti-Cu Dissimilar Joint: Effect of Microstructure and Volta Potential, Materials 11 (2018) 1820.

[42] E. Rahimi, A. Rafsanjani-Abbasi, A. Imani, A. Davoodi, TiO2/Cu2O coupled oxide films in Cl− ion containing solution: Volta potential and electronic properties characterization by scanning probe microscopy, Mater. Chem. Phys. 212 (2018) 403–407.

[43] X. Wan, X. Lu, L. Sun, M. Chen, N. Ta, W. Liu, Q. Chen, L. Chen, J. He, P. Jiang, X. Bao, Interface-enhanced thermoelectric output power in CrN/SrTiO3−x heterostructure, J. Energy Chem. 64 (2022) 16–22.

[44] P. Kumar, J.V. Gajjar, B.R. Mehta, D.R. Roy, 2D bilayer chromium pnictogens as a metallic material under DFT investigation through their structural, vibrational, electronic, and elastic properties, Solid State Commun. 390 (2024) 115614.

[45] H.B. Michaelson, The work function of the elements and its periodicity, J. Appl. Phys. 48 (1977) 4729–4733.

[46] E. Rahimi, R. Offoiach, M. Lekka, L. Fedrizzi, Electronic properties and surface potential evaluations at the protein nano-biofilm/oxide interface: Impact on corrosion and biodegradation, Colloids Surf. B: Biointerfaces 212 (2022) 112346.

[47] Z. Zhang, J.T. Yates Jr., Band Bending in Semiconductors: Chemical and Physical Consequences at Surfaces and Interfaces, Chem. Rev. 112 (2012) 5520–5551.

[48] M. Cedeño-Vente, J. Manríquez, G. Mondragón-Rodríguez, N. Camacho, A. Gómez-Ovalle, J. Gonzalez-Carmona, J. Alvarado-Orozco, D. Espinosa-Arbelaez, Application of a transmission line model to evaluate the influence of structural defects on the corrosion behavior of arc-PVD CrN coatings, Ceram. Int. 47 (2021) 20885–20899.

[49] A. Lippitz, T. Hübert, XPS investigations of chromium nitride thin films, Surf. Coat. Technol. 200 (2005) 250–253.

[50] A. Hughes, C. Easton, T. Gengenbach, M. Biesinger, M. Laleh, Interpretation of complex x-ray photoelectron peak shapes. II. Case study of Fe 2p3/2 fitting applied to austenitic stainless steels 316 and 304, J. Vac. Sci. Technol. A 42 (2024).

[51] D. Zhang, X. Zuo, Z. Wang, H. Li, R. Chen, A. Wang, P. Ke, Comparative study on protective properties of CrN coatings on the ABS substrate by DCMS and HiPIMS techniques, Surf. Coat. Technol. 394 (2020) 125890.

[52] Q. Ye, Y. Li, M. Zhang, S. Zhang, Y. Bi, X. Gao, Y. He, Electrochemical behavior of (Cr, W, Al, Ti, Si) N multilayer coating on nitrided AISI 316L steel in natural seawater, Ceram. Int. 46 (2020) 22404–22418.

[53] E. Rahimi, K. Zhang, A. Kosari, N. Van den Steen, A. Homborg, H. Terryn, A. Mol, Y. Gonzalez-Garcia, Atmospheric corrosion of iron under a single droplet: A new systematic multi-electrochemical approach, Corros. Sci. 235 (2024) 112171.

[54] A. Herwadkar, W.R.L. Lambrecht, Electronic structure of CrN: A borderline Mott insulator, Phys. Rev. B 79 (2009) 035125.

[55] M.T. Greiner, Z.-H. Lu, Thin-film metal oxides in organic semiconductor devices: their electronic structures, work functions and interfaces, NPG Asia Mater. 5 (2013) e55-e55.

[56] N.S. Mansoor, A. Fattah-alhosseini, H. Elmkhah, A. Shishehian, Electrochemical behavior of TiN, CrN and TiN/CrN nanostructured coatings on the nickel-chromium alloy used in dental fixed prosthesis, J. Asian Ceram. Soc. 8 (2020) 694–710.

[57] I. Iso, 14577 Metallic Materials—Instrumented Indentation Test for Hardness and Materials Parameters, ISO, Vernier, Geneva, 2002.

[58] E. Broitman, A. Ruellan, R. Meeuwenoord, D. Nijboer, V. Brizmer, Comparison of Various Conversion Layers for Improved Friction Performance of Railway Wheel-End Bearings, Coatings 13 (2023) 1980.
[59] L. Shan, Y. Wang, J. Li, X. Jiang, J. Chen, Architecture of multilayer Cr/CrN coatings for wear protection in seawater: Cr/CrN ratio and total thickness, Tribology Trans. 58 (2015) 914–923.
[60] F. Jasempoor, H. Elmkhah, O. Imantalab, A. Fattah-alhosseini, Improving the mechanical, tribological, and electrochemical behavior of AISI 304 stainless steel by applying CrN single layer and Cr/CrN multilayer coatings, Wear, 504- 505 (2022) 204425.